



# Enhancement of room temperature ferromagnetic behavior of Co-doped ZnO nanoparticles synthesized via sol–gel technique

Niraj K. Singh<sup>1</sup> · Vaibhav Koutu<sup>1,2</sup> · M. M. Malik<sup>1</sup>

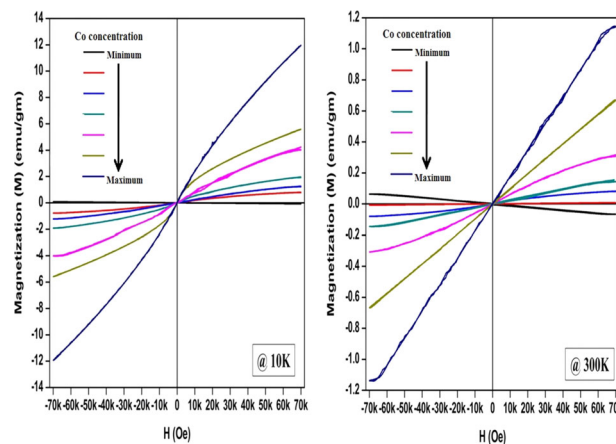
Received: 30 November 2018 / Accepted: 19 April 2019 / Published online: 27 April 2019  
© Springer Science+Business Media, LLC, part of Springer Nature 2019

## Abstract

Zn<sub>1-x</sub>Co<sub>x</sub>O ( $x = 0, 0.001, 0.005, 0.01, 0.02, 0.04, \text{ and } 0.06$ ) nanoparticles (NPs) were synthesized by sol–gel method. Ingestion of Co<sup>2+</sup> ions in the ZnO crystal lattice created defects without disturbing the original crystal structure of ZnO. This is confirmed by the X-ray diffraction (XRD) studies and is also observed in the photoluminescence (PL) emission study where the Co-doped ZnO NPs have shown emissions in the green and yellow-orange regions of visible spectrum. XRD and transmission electron microscopic (TEM) analysis showed reduction in crystallite size from 29 to 14.5 nm and from 51 to 36 nm, respectively, with increase in Co<sup>2+</sup> ions concentration. Optical absorption spectroscopic studies (UV-visible spectroscopy) of these samples show significant peak shift towards higher energy (blue shift), which is in accordance with the Kubo's theory. Magnetic properties were studied using quantum designed vibrating sample magnetometry (VSM), which confirmed that Co-doped ZnO NPs exhibit room temperature ferromagnetism (RTFM) for the samples having high Co concentration. With these notable properties, this study suggests that Co-doped ZnO NPs may be useful in the field of optoelectronic devices and memory-storage devices as well.

## Graphical Abstract

The graphical abstract for the manuscript shows that, with increase in cobalt (Co) doping concentration, the magnetization increases significantly at low temperature (10 K) and room temperature (300 K).



✉ Vaibhav Koutu  
vkoutu@gmail.com

<sup>1</sup> Nanotechnology Research Laboratory, Department of Physics & Nano Science and Engineering, Maulana Azad National Institute

of Technology, Bhopal, MP, India

<sup>2</sup> Department of Bio-Medical Engineering, Shri Govindram Seksaria Institute of Technology and Science, Indore, MP, India

## Highlights

- Co-doped ZnO nanoparticles were synthesized using Sol-gel technique and characterized.
- Effect of Co-doping on the structural, optical and magnetic properties are discussed in detail.
- With increase in Cobalt doping concentration, crystallite size as well as particle size of as-prepared Co-doped ZnO samples decreases, which in turn causes increase in the crystallite strain.
- From the Magnetization-Hysteresis (M-H) curve analysis, it is revealed that Room temperature ferromagnetism (RTFM) is present in Co-doped ZnO NPs with high values of coercive field ( $H_c$ ).

**Keywords** Sol-gel · Strain · Defects · Vacancies · RTFM · DMS

## 1 Introduction

Nano-dimensioned zinc oxide (ZnO) has become a prominent material of research interest in past few years due to its vast range of industrial applications in opto-electronics (nano-piezotronics, ultraviolet (UV) detectors, transparent solar cells, chemical sensors, and gas sensors) [1], medicinal material (drug carriers) [2, 3], transparent UV protection films, and low voltage and short-wavelength electro-optical devices [4, 5] and spintronics [6]. The reason for this versatility of ZnO is attributed to its wide band gap (3.37 eV), large exciton binding energy (60 MeV), and also it possess structure-dependent properties [1]. Among these applications, recently, the utilization of ZnO as a spintronic material has attracted significant attention of the researchers due to its ability to replace conventional semiconductor electronics for information technology devices [7, 8]. In this context, the most important type of spintronic material is the diluted magnetic semiconductors (DMSs). Though, it was reported that undoped ZnO exhibits ferromagnetic (FM) properties at room temperature [9, 10], still the room temperature saturation magnetization is extremely small to be utilized for practical application. In order to enhance the magnetization and its utilization in DMS and spintronics, doping with transition metal (TM) ions (such as Ni, Co, Mn, and Ni) was employed to adjust the energy band gap of ZnO, which in turn improves its magnetic properties [1, 11–13]. It was observed that the substitution of  $Zn^{2+}$  ion in ZnO crystal lattice by a 3d TM ion introduces FM behavior in the ZnO mainly by intrinsic defects or impurity phases, while preserving its semiconducting properties [1, 11]. Most important attention is emphasized on the fact that the FM properties should only be intrinsic and not due to presence of any of dopant magnetic clusters [14]. These parameters have enabled the researchers to enhance the room-temperature ferromagnetism (RTFM) in TM-doped ZnO for their advanced applications in spintronic devices [1, 11].

Both undoped and TM-doped ZnO nanoparticles (NPs) have been synthesized chemically using techniques, such as co-precipitation, sonochemical, hydrothermal, and sol-gel methods, as well as via physical methods such as physical vapor deposition, chemical vapor deposition, spray pyrolysis,

pulse-laser deposition, and flame decomposition of metal-organic compounds and combustion techniques [15–18]. Among these available methods, sol-gel technique is considered as most suitable technique for NP synthesis because of the advantages like low synthesis temperature, high purity, homogenous particle size distribution, and low capital costs [12]. Among various TM dopants reported so far, Cobalt (Co) is considered as the best dopant material because of its abundant electron states, large solubility in the ZnO matrix, and also cobalt has a similar ionic radius (0.58 Å) to that of Zn (0.60 Å) [15, 19]. Also, the doping of  $Co^{2+}$  increased the magnetization values because  $Co^{2+}$  in the half-filled 3d shell has five spins, which normally gives a maximum dipole moment value of 3  $\mu_B$  per Co ion [11].

After extensive literature survey, it was discovered that the TM ions doped-ZnO NPs still continues as an open topic for further exploration in RTFM. In this work, the authors report an investigation on structural, morphological, optical, and magnetic properties of ZnO NPs doped with cobalt ( $Co^{2+}$ ) ions synthesized via sol-gel method [20]. Here cobalt ( $Co^{2+}$ ) has been selected as dopant material because of the two reasons: (i)  $Co^{2+}$  ions are stable in alcoholic medium and they can replace zinc ion without creating cationic vacancy, (ii) these ions can occupy tetrahedral sites very easily that can in turn induce many different structural and optical properties [20]. The effect of cobalt incorporation on structural and optical properties was investigated using X-ray diffraction (XRD), transmission electron microscopy (TEM), UV-visible spectroscopy, photoluminescence (PL) spectroscopy, and quantum designed superconducting quantum interference device (SQUID) vibrating sample magnetometer (VSM) techniques.

## 2 Experimental procedure

Co-doped ZnO  $\{x = 0, 0.001, 0.005, 0.01, 0.02, 0.04, \text{ and } 0.06\}$  samples were prepared by sol-gel technique by using zinc acetate dehydrate ( $Zn(CH_3COO)_2 \cdot 2H_2O$ ) as zinc precursor and cobalt acetate tetrahydrate ( $Co(CH_3COO)_2 \cdot 4H_2O$ ) as cobalt precursor and monoethanolamine (MEA) as a

**Table 1** Details of synthesized undoped and Co-doped ZnO ( $\text{Zn}_{1-x}\text{Co}_x\text{O}$ ) samples

S.No.	Sample	Molar ratio		Reaction temperature	Calcination temperature	Heating time
		Zinc acetate ( $1-x$ )	Cobalt acetate ( $x$ )			
1.	CP0	1	0	65 °C	500 °C	4 h
2.	CP1	0.999	0.001	65 °C	500 °C	4 h
3.	CP2	0.995	0.005	65 °C	500 °C	4 h
4.	CP3	0.99	0.01	65 °C	500 °C	4 h
5.	CP4	0.98	0.02	65 °C	500 °C	4 h
6.	CP5	0.96	0.04	65 °C	500 °C	4 h
7.	CP6	0.94	0.06	65 °C	500 °C	4 h

stabilizer and complexing agent. All the chemicals and precursors were purchased from Sigma-Aldrich (99.99% pure). Equi-volume ethanolic solutions of zinc acetate (0.2 M) and cobaltous acetate were prepared using ethanol as a reaction medium. Following the standard rules of stoichiometry, different concentrations of cobalt acetate and zinc acetate were mixed thoroughly by proper stirring at 500 rpm for 1 h. After that, a calculated amount of MEA was added drop-wise to the stirring solution, which resulted in clear, transparent, and homogeneous solution. The molar ratio of MEA to metal ions was maintained at 1.0. The above complex solution then continuously stirred at 65 °C for 3 h under constant speed and the as-prepared solution is then aged for 48 h at room temperature to obtain a homogenous gel. The gelled samples were then dried at 140 °C for 12 h and finally calcined at 500 °C for 4 h under air ambience. The obtained material was then finely grinded using agate mortar and pestle to obtain the desired ZnO samples. Table 1 shows the details of the prepared samples.

All the characterizations were performed at room temperature. The crystal structure and purity of the samples was characterized using X-ray diffractometer Rigaku MiniFlex II (1.54 Å Cu-K $\alpha$  radiation) in the range 20°–80° ( $2\theta$ ) at scan rate of 0.5° min<sup>-1</sup>. Morphology of the samples was studied by 120 kV High-Resolution Transmission Electron Microscope (JEM-1400, Jeol, Japan). Optical absorption spectrum of the samples was obtained by Perkin Elmer LAMBDA 25 UV–Visible spectrophotometer, while emission property was characterized by Hitachi F-7000 PL Spectrophotometer. Magnetic measurements were carried out using quantum designed SQUID VSM Magnetometer (Model: MPMS-3, Make: Quantum Design Inc., USA).

## 3 Results and Discussion

### 3.1 Crystal structure analysis: XRD

The structural information of pure ZnO and Co-doped ZnO samples were analyzed by XRD patterns using Rietveld

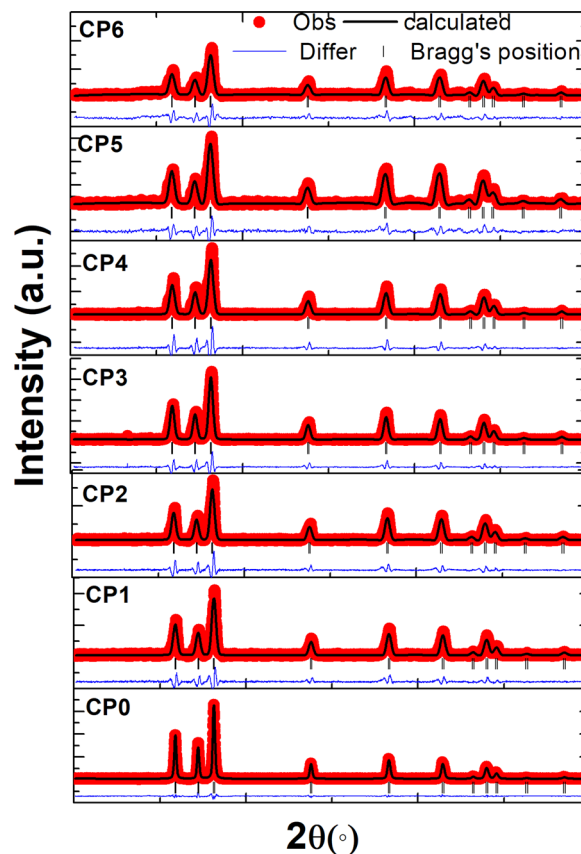


**Fig. 1** Rietveld refinement profiles of X-ray diffraction data of the undoped and Co-doped ZnO samples. The red lines represent the observed data while the solid black line through the red line shows the calculated profile. The difference pattern of the observed data and calculated profile (blue line) is provided below Bragg reflections

refinement method and are represented in Fig. 1. All the diffraction peaks in the obtained patterns are well matched with the JCPDS file #36-1451 of the standard ZnO and can be indexed corresponding to the hexagonal reflections of the wurtzite ZnO. No characteristic peaks of the impurity were observed for all the samples.

The X-ray data were from the XRD pattern (Fig. 1), no characteristic phases of cobalt oxide, cobalt traces, or any other impurity phases were observed which suggest that Co

**Table 2** Calculated values of average crystallite size for the ZnO samples by UDM (W-H plot), Scherrer formula and FESEM and strain

Sample	Average crystallite size		Strain ( $\epsilon$ ) (from W-H plot)	Strain along $c$ axis ( $\epsilon_{zz}$ ) (from Eq. 3) (%)	Lattice parameters		
	UDM (W-H plot)	Scherrer formula			$a$ (Å)	$c$ (Å)	Volume ( $V$ ) (in Å <sup>3</sup> )
CP0	29.1 nm	39.7 nm	$1.30 \times 10^{-3}$	0.91	3.2472	5.2015	47.496
CP1	19.0 nm	24.9 nm	$-1.32 \times 10^{-3}$	1.30	3.2474	5.2017	47.504
CP2	17.6 nm	23.9 nm	$-1.35 \times 10^{-3}$	1.40	3.2497	5.2058	47.603
CP3	17.5 nm	23.7 nm	$-1.47 \times 10^{-3}$	1.51	3.2502	5.2058	47.623
CP4	15.7 nm	21.3 nm	$-1.7 \times 10^{-3}$	1.59	3.2504	5.2068	47.638
CP5	15.0 nm	20.3 nm	$-2.1 \times 10^{-3}$	1.75	3.2509	5.2072	47.657
CP6	14.7 nm	20.2 nm	$2.45 \times 10^{-3}$	1.88	3.2520	5.2082	47.698

FESEM field-emission scanning electron microscopy, UDM Uniform Deformation Model

is substituted at Zn sites and the wurtzite crystal lattice remained intact. Also, with increase in  $\text{Co}^{2+}$  ion concentration, the diffraction peaks show broadening and slight shift toward lower Bragg angle ( $2\theta$ ), which represents the reduction in crystallite size as well as presence of uniform strain [15]. The average crystallite size ( $d$ ) of as-prepared samples was calculated using Scherrer's equation [15, 17, 21, 22],

$$d = \frac{0.9\lambda}{\beta \cos\theta} \quad (1)$$

where  $\lambda$  is the incident radiation wavelength ( $\lambda = 1.54 \text{ \AA}$ ),  $\beta$  is the peak full width at half maxima, and  $\theta$  is the Bragg's angle. Lattice parameters ( $a$  and  $c$ ) were determined using the formula:

$$\sin^2\theta = \frac{\lambda^2}{4} \left[ \frac{4}{3} \left( \frac{h^2 + hk + k^2}{a^2} \right) + \frac{l^2}{c^2} \right] \quad (2)$$

where  $h$ ,  $k$ , and  $l$  are the Miller indices [15, 17, 21, 22]. Variation in the lattice parameters ( $a$  and  $c$ ) and the corresponding unit cell volume ( $V = 0.866a^2c$ ) of the as-prepared samples were calculated and are represented in Table 2.

The cell volume of Co-doped ZnO NPs was found to increase with increase in  $\text{Co}^{2+}$  ion concentration, which is in accordance with the Vegard's law [11]. The ratio of lattice parameters ( $c/a$ ) for all Co-doped ZnO NPs had the value 1.73, which is slightly higher than that of standard value of ZnO ( $c/a = 1.62$ ), which suggests that the doping of  $\text{Co}^{2+}$  takes place by producing some lattice defects but without affecting the overall structure of ZnO.

The nature of microstrain ( $\epsilon_{zz}$ ) in the samples along  $c$  axis was calculated and tabulated in Table 2, using the equation

$$\epsilon_{zz} = \left( \frac{c - c_0}{c_0} \right) \times 100 \quad (3)$$

where  $c_0$  is the unstrained lattice parameter and  $c$  is the lattice parameter calculated from the XRD data [15]. The relation between crystallite size and strain could be explained using Williamson–Hall (W-H) method [15] given by:

$$\beta \cos\theta = k\lambda/d + 4\epsilon \sin\theta \quad (4)$$

This equation represents the Uniform Deformation Model (UDM), which assumes that the strain is uniform in all crystallographic directions [15]. The values of crystallite size calculated from both Debye–Scherrer formula and W-H analysis are tabulated in Table 2. From Table 2, it was observed that the crystallite size of the Co-doped ZnO NPs reduces with increase in the  $\text{Co}^{2+}$  ion concentration. This observation is well supported by the corresponding increase in the value of strain ( $\epsilon$ ). Positive value of  $\epsilon_{zz}$  accounts for the tensile strain and is in good agreement with the obtained from W-H analysis [1]. The crystallite size ( $d$ ), calculated using Scherrer's formula and W-H analysis, decreases with increase in  $\text{Co}^{2+}$  doping entailing that  $\text{Co}^{2+}$  ions inhibit the nucleation and growth rate of nanocrystals. Gandhi et al. [11] reported that substitution of  $\text{Co}^{2+}$  in an interstitial position affects the concentration of the interstitial Zn, O, and Zn vacancies, which in turn is reflected via changes in Bragg's angle ( $2\theta$ ), broadening of peak width ( $\beta$ ), and reduction of crystallite size.

### 3.2 Morphological analysis: TEM

TEM images (Fig. 2a–g) shows the morphology of the as-prepared undoped and Co-doped ZnO samples (CP0–CP6). All the samples were analyzed at 120 kV accelerating voltage, and for better analysis, all the samples were studied at 50 nm scale. TEM images show the presence of homogenous, well-dispersed particles having well-defined grain boundary. Figure 2a shows that undoped ZnO sample have spherical-like morphology with well-defined grain boundaries and no sign of agglomeration (shown in center). It is

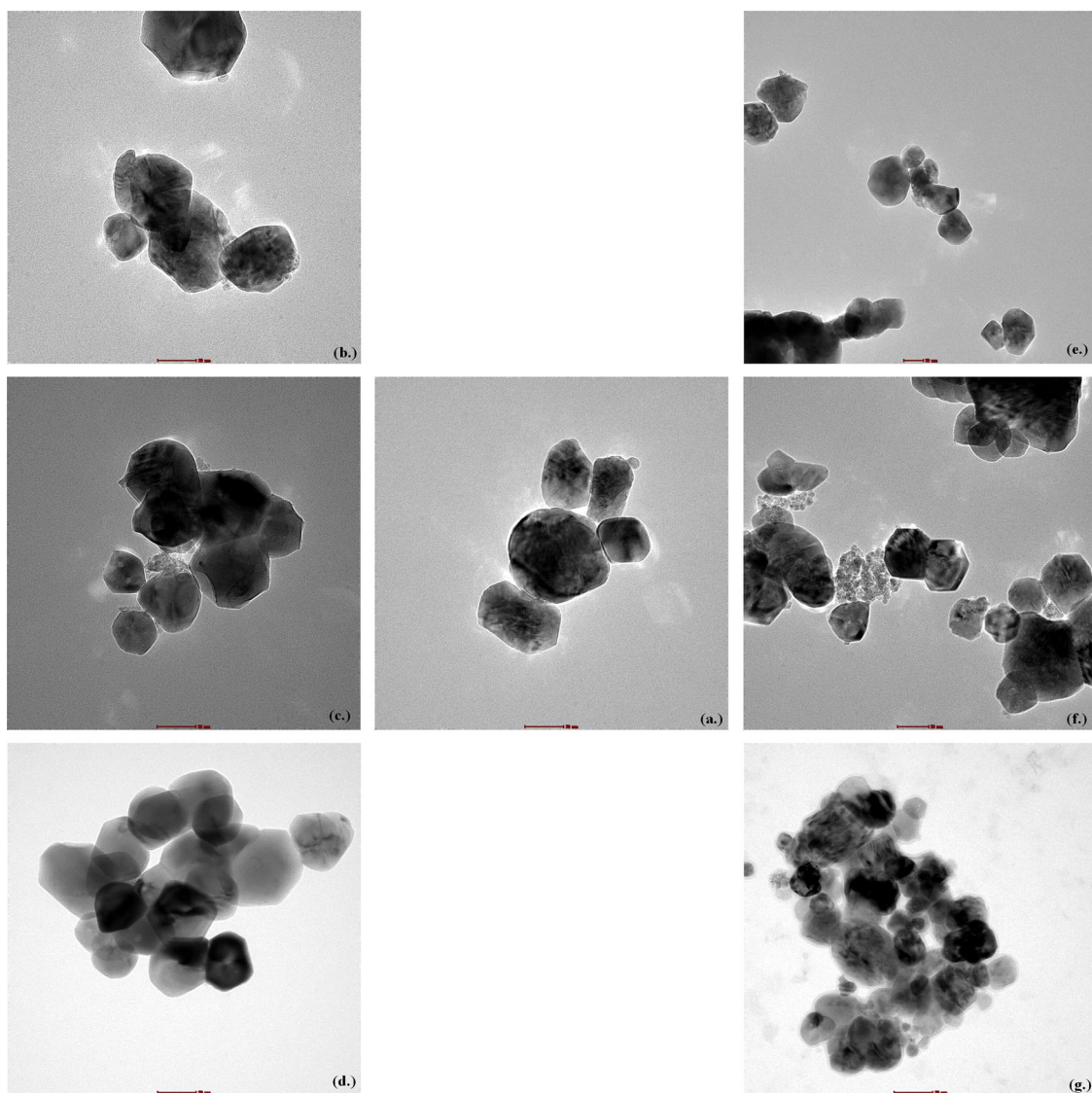


**Fig. 2** Transmission electron microscopic images showing morphology of as-prepared undoped and Co-doped ZnO samples (a–g: CP0–CP6, respectively)

observed that the doping of  $\text{Co}^{2+}$  does not radically alter the shape of the particles (Fig. 2b–g).

Slight variation in the morphologies is observed that may be due to the presence of  $\text{Co}^{2+}$  ions in the ZnO lattice, which would have produced some strain/stress in the ZnO matrix and resulted in slight variation of the seed morphology, though it can be observed that particles are attracted to each other which may be attributed to the magnetic property of  $\text{Co}^{2+}$  ions that had caused particles to agglomerate. But it can also be seen that there is no sign of boundary diffusion which suggests that the particles formed are of uniform shape and are well dispersed. The agglomeration of particles increases with increase in  $\text{Co}^{2+}$  doping concentrations as are clearly revealed in Fig. 2b–g. The average particle size calculated from TEM images ranges

from 51 nm (for undoped ZnO sample) to 29 nm (for CP8) (enlisted in section 4.5, Table 4). This shows that, with increase in  $\text{Co}^{2+}$  concentration, average particle size of Co–ZnO NPs reduces when compared to undoped ZnO surmising small grain growth of doped samples.

Figure 3a, b represents the selected area electron diffraction (SAED) pattern of undoped and Co-doped ZnO (CP6) samples. From the SAED pattern, it can be inferred that the particles are of nano-dimensions and are homogenous in nature [23]. The diffraction rings obtained from SAED pattern can be indexed to the reflections of hexagonal wurtzite structure of ZnO. From Fig. 3b, it can be observed that no other rings belonging to Co-oxide or its associated phases are obtained that suggests the incorporation of  $\text{Co}^{2+}$  ions in ZnO lattice site without any growth or

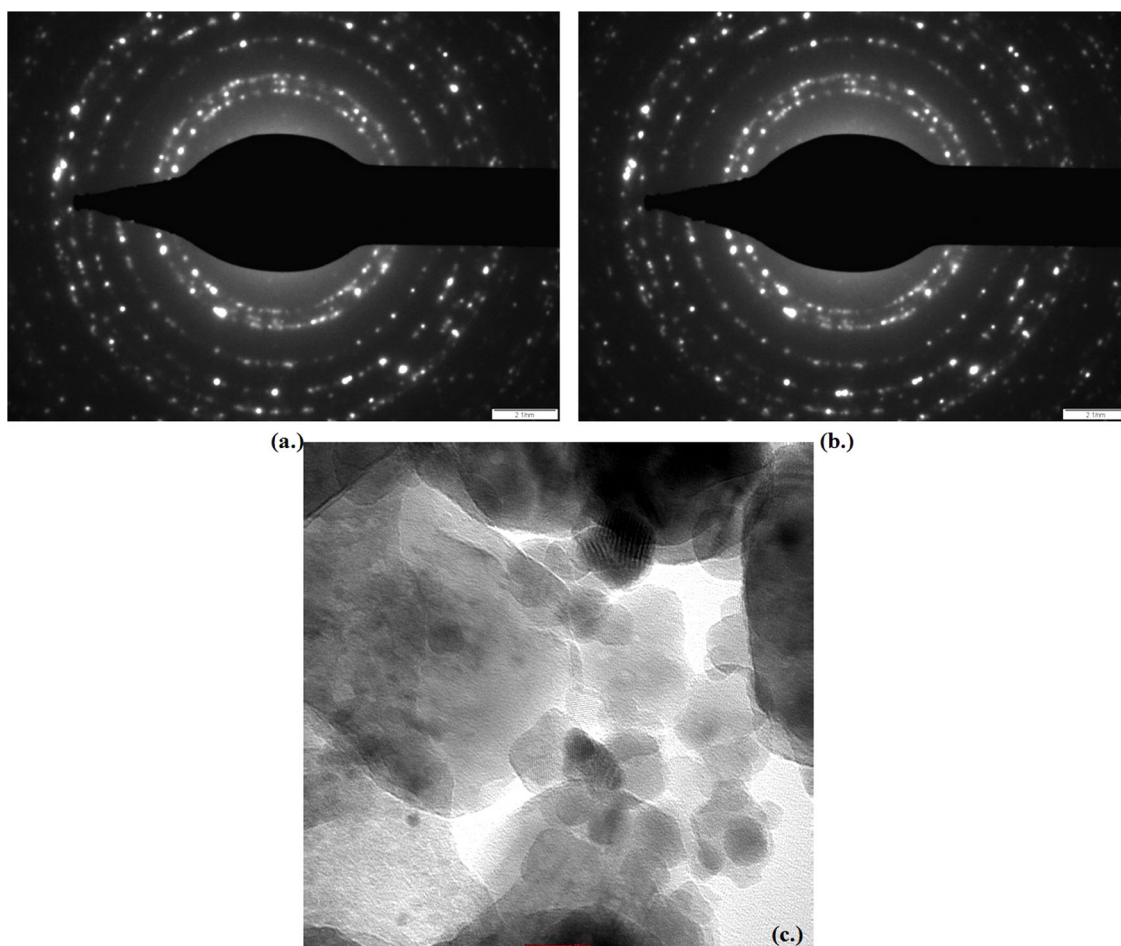


**Fig. 3** **a, b** Selected area electron diffraction pattern of undoped and Co-doped samples, respectively. **c** Transmission electron microscopic image showing different planes of Co-doped sample

development of any extra plane in the crystalline structure of ZnO [23]. High-resolution TEM (HRTEM) image of CP6 sample (Fig. 3c) reveals the lattice spacing of 0.50 nm, which corresponds to the interplanar spacing of wurtzite ZnO (002) plane.

### 3.3 Optical emission analysis: PL spectroscopy

Optical emission of the undoped and Co-ZnO samples was studied by room-temperature PL spectroscopy. The samples were excited at 325 nm excitation wavelength and the emission spectrum of each sample was plotted, as shown in Fig. 4.

According to the literature [15, 20, 24], increase in number of emission peaks represents an increase in defect levels in the material. The position of the peaks provides information about the depth and type of defects in the material [20]. From the emission spectra (Fig. 4), the emissions can be categorized into two groups: (i) a near-band edge emission around 380 nm (which originates from the recombination of free excitons [24]) is observed for

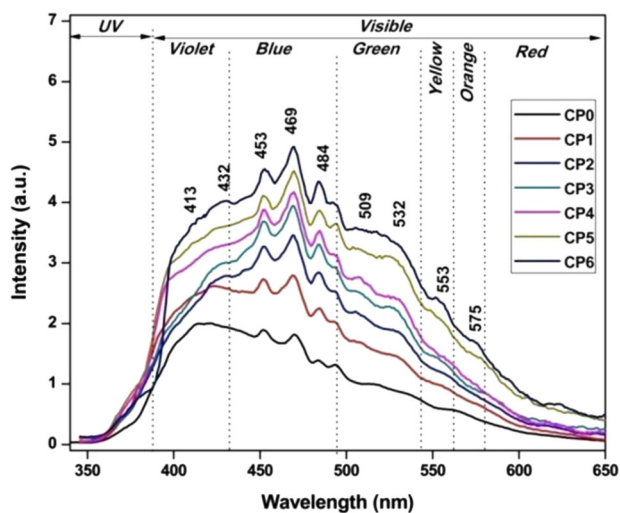


**Fig. 4** Emission spectrum of the undoped and Co-doped ZnO nanoparticles excited at 325 nm

undoped ZnO and CP1 samples only, (ii) major emission peaks in the visible region centered around 400–435 nm

(violet region), 450–490 nm (blue region), 510–532 nm (green region), and around 553 nm (yellow region). Violet emissions arise due to the presence of zinc-related defects, i.e., zinc interstitial or zinc vacancy where transition of electron between zinc defect level and valance band causes the violet luminescence [25]. Blue and green emissions arise due to lattice defects developed as a result of compressive strain produced at the intrinsic crystal lattice [15, 24], which leads to the formation of oxygen and zinc vacancies and interstitials simultaneously causing transitions of energy from conduction band or zinc interstitials to the vacant zinc sites resulting in blue emission, while the same originating from deep levels cause green emissions [15, 25]. Emission peaks around 553 nm (yellow region) is observed for Co-doped ZnO samples (CP1–CP6) that arise because of oxygen interstitials [15]. It may be inferred that high  $O^-/O^{2-}$  ion concentration leads transitions of holes from conduction bottom to the oxygen interstitial site emitting yellow emissions around 2.2 eV [15, 24]. CP5 and CP6 samples show emissions in orange region also (575 nm), which are attributed to the increased oxygen vacancies along with zinc interstitials [24]. The PL spectra of the ZnO samples show high intensity emissions in broad visible region with respect to the increasing  $Co^{2+}$  ion concentration which infers that these NPs could be utilized for opto-electronic devices and UV sensor applications.

### 3.4 Magnetization measurements: quantum designed SQUID VSM magnetometer

The magnetization measurements of the undoped and Co-ZnO samples were performed using a quantum designed SQUID VSM magnetometer. The magnetization–hysteresis curves (M-H) were measured within magnetic fields ( $H$ ) range of  $\pm 70$  kOe (70 T) for different temperatures ranging from 10 K to 300 K and are represented in Fig. 5a. Also, temperature-dependent magnetic properties, i.e., magnetization–temperature (M-T) measurements for zero field-cooled (ZFC) and field-cooled (FC) processes were measured at low magnetic field (500 Oe) in the temperature range from 10 K to 300 K (shown in Fig. 6).

Figure 5 shows the M-H curves of the undoped and Co-doped ZnO NPs measured between  $\pm 70,000$  Oe (7 T) magnetic field at 10 K and 300 K, respectively. The values of coercive field ( $H_c$ ) and remnant magnetization ( $M_r$ ) for undoped and Co-doped ZnO samples were calculated from the M-H curves and mentioned in Table 3. From the Table 3, it was revealed that  $H_c$  value increases with increase in the  $Co^{2+}$  concentration and decreases with increasing temperature. This may be attributed to the thermal effects causing alignment of the magnetic domains [26].

The M-H curves of the Co-doped ZnO NPs show nearly S-shape behavior at low temperature region while they

exhibit approximate linear field dependence at room temperature. From the M-H curves, it was observed that the undoped ZnO shows diamagnetic behavior, while for Co-doped NPs the magnetization increases with increase in Co doping. Many researchers have reported that pure ZnO has characteristic diamagnetic behavior [1, 13, 14], and similar finding was observed in this case also. It was also interesting to observe that the magnetization does not saturate even at 7 T, which suggests that there exists an anti-FM contribution along with the FM interactions within the doped samples [26]. From the M-H curves, it can be inferred that all Co-doped samples exhibit FM behavior with hysteresis loops. This was obvious and is attributed to the tendency of Co magnetic moments that align significantly at lower temperature [27]. Though the magnetization at RT is lower than that of at 10 K, still it is much higher (by order of  $\sim 10^2$  and more) than those reported by researchers previously [13, 14, 24–28].

Magnetic behavior of all samples at low temperature (between 10 K and 300 K at 500 Oe) was studied by ZFC and FC measurement. The M-T plots shown in Fig. 6 reveal that FC and ZFC curves bifurcate at different temperatures for Co-doped ZnO samples. The bifurcation of the FC and ZFC curves starts at around 20 K, which indicates the onset of magnetic ordering in the doped ZnO samples [24]. High value of magnetization at low temperature is the primary characteristic of DMS material [24, 26]. Hence, it can be inferred that the doped ZnO NPs consists of both FM and paramagnetic domains at low temperature and is directly proportional to the doping concentration. This can also be observed from the M-H curves of the NPs (Fig. 5a).

Many researchers have deliberated several theories to explain the origin of FM in TM-doped ZnO NPs, but still the exact reason is unexplained [1, 3]. From the survey of many reports, it was understood that the possible reasons for FM in TM-doped ZnO NPs are: (i) the interrelationship between defects and magnetism, (ii) secondary phases (extrinsic defects) in the parent crystal lattice [29, 30], and (iii) intrinsic defects, such as Zn vacancy ( $V_{Zn}$ ), interstitial defects, and oxygen vacancy ( $V_o$ ) [23]. In the present study, FM due to extrinsic factors cannot be justified because the XRD and TEM studies clearly show the absence of any secondary and/or impurity phase in all of the Co-doped samples. Thus it can be stated that the cause of RTFM in this case is only due to internal defects. Similar results were obtained by Guruvammal et al. [23] also, whose report suggests that the origin of RTFM was due to the exchange interaction between the localized spin of  $Co^{2+}$  electron moments resulting from oxygen vacancies ( $V_o$ ). The addition of  $Co^{2+}$  ions in ZnO lattice increases the oxygen vacancies, which in turn increase the carrier density ( $e^-$ ) and their interaction causes all the spins of  $Co^{2+}$  ions to

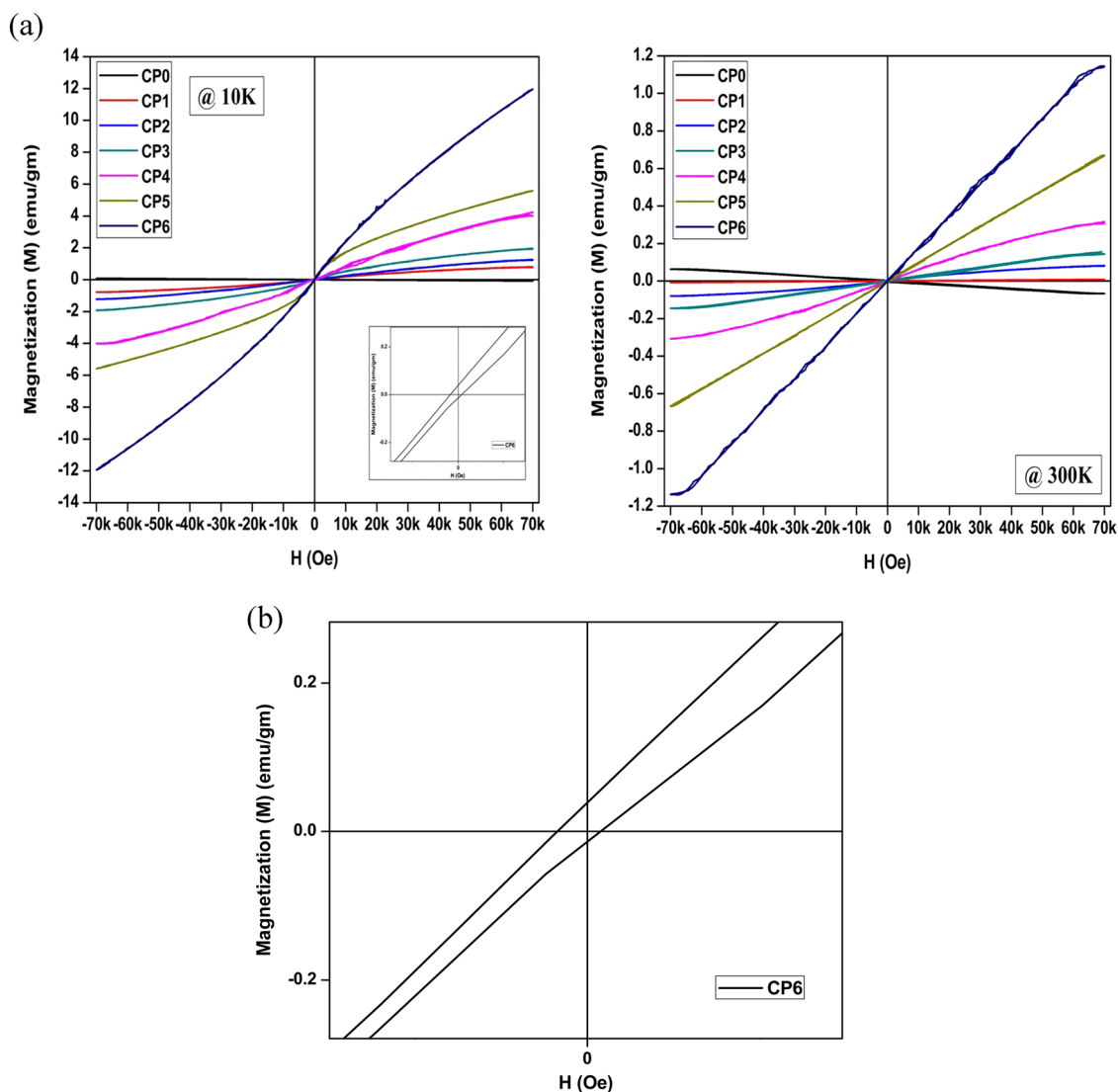


**Fig. 5** **a** Magnetization–hysteresis (M-H) curves of undoped and Co-doped ZnO nanoparticles measured at: 10 K, and 300 K. **b** Magnified inset (of **a**) for sample CP6

align either in same direction or spin up/down, thus resulting in onset of FM in Co-doped ZnO samples [23]. These results are in good agreement with PL results also.

From the above discussion, it can be concluded that an increase in magnetization is associated mainly with the increase in oxygen vacancies due to the existence of magnetic  $\text{Co}^{2+}$  ions within ZnO lattice, leading to the enhancement of the FM behavior in Co-doped ZnO NPs [3, 31, 32]. Hence, it can be suggested that these Co-doped NPs may find application in memory-storage devices also.

### 3.5 Optical absorbance analysis: UV-visible spectroscopy

Effect of Co-doping on the optical absorbance of ZnO was also studied by UV-visible spectroscopy done in the range

200–650 nm. For comprehensible observation, absorbance spectrum of the CP0, CP1, CP3, and CP6 samples with respect to the incident wavelength ( $\lambda$ ) is represented and is shown in Fig. 7 (inset).

From the absorbance spectrum (Fig. 7 (inset)), it was inferred that the absorption spectra show blue shift in the absorption edge of the Co-doped ZnO samples with increase in  $\text{Co}^{2+}$  ion concentration and also with respect to undoped ZnO sample. The shape and width of the absorbance peak gives a general idea about the particle size distribution in the sample [15]. According to Kubo theory [15], the absorption band shifts to blue region of visible spectrum with reduction in particle size and consequently increases the band gap. It has also been reported in the literature [15, 33, 34] that, for nano-dimensioned particles, the separation of energy level occurs as the interaction



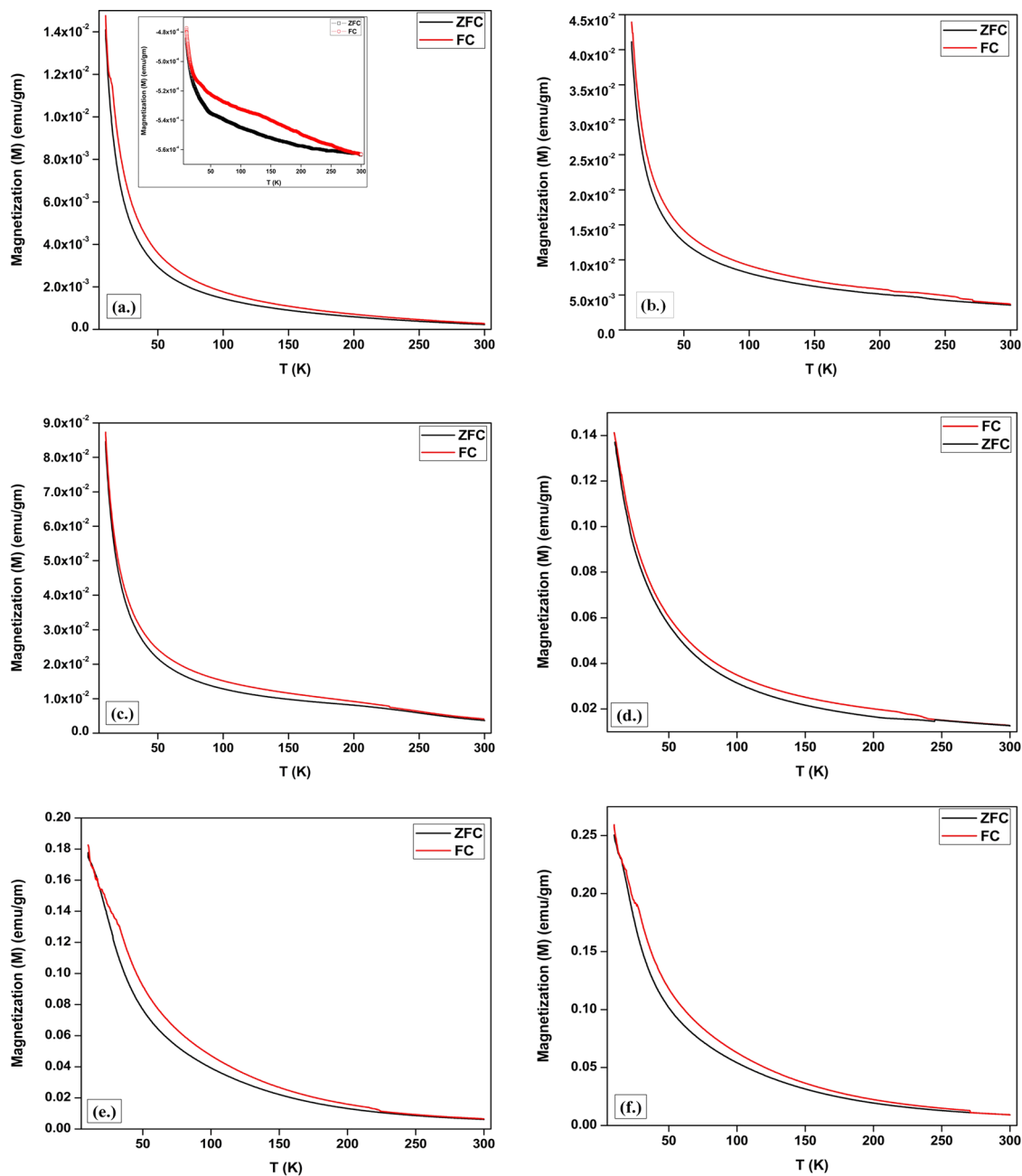


**Fig. 6** a–f Magnetization–temperature ( $M$ - $T$ ) curves of Co-doped ZnO nanoparticles (NPs) measured in temperature range 10–300 K at 500 Oe magnetic field. (Inset:  $M$ - $T$  curve of undoped ZnO NPs)

**Table 3** Remnant magnetization ( $M_r$ ) and coercive field ( $H_c$ ) values calculated from  $M$ - $H$  curves (@10 K)

Sample	$M_r$ (emu/gm)	$H_c$ (Oe)
CP1	$7.85 \times 10^{-4}$	140
CP2	$8.66 \times 10^{-4}$	194
CP3	$1.12 \times 10^{-3}$	286
CP4	$1.43 \times 10^{-3}$	342
CP5	$4.46 \times 10^{-3}$	400
CP6	$4.78 \times 10^{-3}$	510

between the atomic energy levels is reduced and quantum effects are dominant. The optical band gap ( $E_g$ ) of the ZnO samples was determined using two methods,

(i) Energy–wavelength equation [15, 35]:

$$E_g = \frac{hc}{\lambda} \quad (5)$$

where  $h$  is the Planck's constant,  $c$  is speed of light, and  $\lambda$  is the absorption wavelength.

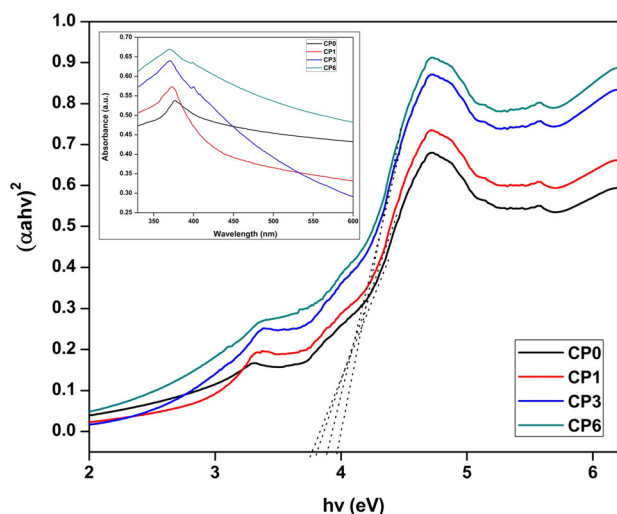


**Fig. 7** Tauc plot of the undoped and Co-doped ZnO samples using absorption spectra fitting method (Inset: Absorbance spectra of the corresponding samples)

**Table 4** Energy band gap of the undoped and Co-doped ZnO NPs calculated from optical absorption spectra

Sample	Absorption edge ( $\lambda$ )	$E_g$ (by energy–wavelength equation $E_g = 1240/\lambda$ ) (in eV)	$E_g$ (by Tauc plot) (in eV)	Average particle size (TEM analysis)
CP0	337 nm	3.67	3.76	51 nm
CP1	334 nm	3.71	3.80	47 nm
CP2	332 nm	3.73	3.84	45 nm
CP3	331 nm	3.74	3.87	43 nm
CP4	329 nm	3.76	3.90	41 nm
CP5	325 nm	3.81	3.92	39 nm
CP6	321 nm	3.86	3.96	36 nm

NP nanoparticle, TEM transmission electron microscopy

(ii) Absorption spectra fitting method (Tauc’s equation) [36]

$$\alpha hv = B(hv - E_g)^n \quad (6)$$

where  $B$  is a constant,  $h\nu$  is the energy of incident photons, and value of  $n$  depends upon the type of transitions (1/2 for allowed direct, 2 for allowed indirect, 3/2 for forbidden direct, and 3 for forbidden indirect transitions),  $E_g$  is the band gap and  $\alpha$  is the absorption coefficient, ( $\alpha = \frac{2.303A}{t}$  where  $A$  is the absorbance obtained from the graph and  $t$  is the sample thickness (in mm)) [15]. Figure 4 shows the variation of  $(\alpha hv)^2$  with respect to incident photon energy ( $h\nu$ ). The optical band gap of the samples was obtained by extrapolating the linear portion of the graph on y axis [15, 37] (Table 4).

From Table 4, it can be observed that, with increase in  $\text{Co}^{2+}$  ion concentration, the samples show blue shift in the

absorption edge that indicates the reduction in particle size and increase in the energy band gap. This is in accordance with the Kubo’s theory [15]. Slight variation in the values of band gap obtained from both the methods are due to the fact that energy–wavelength method considers only the absorption edge of the spectra, hence the role of overall particles in the band gap is not taken into account, because at absorption edge, only the largest particles contribute to the absorbance, while Tauc’s equation determines the true optical band gap of the material [15, 38]. The results obtained are in accordance with the TEM analysis.

## 4 Conclusion

Undoped and Co-doped ZnO NPs were successfully prepared in ethanolic medium by sol–gel method, which resulted in reduction of the average crystallite size (from 29 to 13 nm) with increase in  $\text{Co}^{2+}$  ion concentration. XRD study reveals that, with increase in  $\text{Co}^{2+}$  ion concentration, the number of defects increases with increase in value of strain. Structural analysis from TEM shows that Co-doped ZnO NPs are spherical in shape with a slight variation from spherical morphology with increasing  $\text{Co}^{2+}$  ion concentration. Absorption studies show blue shift in the absorption edge due to which energy band gap increases from 3.76 to 3.93 eV with respect to increase in  $\text{Co}^{2+}$  ion concentration. This is in accordance with the Kubo theory. Room temperature PL spectra show broad and intense emissions in the visible region that are related to  $V_o$  defects, which are directly proportional to the  $\text{Co}^{2+}$  ion concentration. VSM studies revealed the presence of RTFM in Co-doped ZnO NPs with high values of coercive field ( $H_c$ ). Results so obtained advocate that these NPs are suitable for applications in optoelectronic devices as well as in memory-storage devices also.

**Acknowledgements** The authors thank Director MANIT Bhopal for providing laboratory and research facilities to carry out the experiments.

**Author contributions** The authors have made the following contributions in the present manuscript: NKS is involved in concept and design, experimental work, and data collection of the manuscript. VK has been involved in the interpretation and analysis of the obtained results and data and also in drafting the manuscript. The corresponding author, MMM has critically revised the manuscript in terms of interpretation and analysis and has given the final approval of the version to be published.

## Compliance with ethical standards

**Conflict of interest** The authors declare that they have no conflict of interest.

**Publisher’s note:** Springer Nature remains neutral with regard to jurisdictional claims in published maps and institutional affiliations.

## References

- Fabbiyola S, Kennedy LJ, Aruldoss U, Bououdina M, Dakhel AA, Vijaya JJ (2015) Synthesis of Co-doped ZnO nanoparticles via co-precipitation: structural, optical and magnetic properties. *Powder Technol* 286:757–765
- Singh S, Barick KC, Bahadur D (2013) Shape-controlled hierarchical ZnO architectures: photocatalytic and antibacterial activities. *CrystEngComm* 15(no. 23):4631–4639
- Basith NM, Vijaya JJ, Kennedy LJ, Bououdina M, Jenefar S, Kaviyaran V (2014) Co-doped ZnO nanoparticles: structural, morphological, optical, magnetic and antibacterial studies. *J Mater Sci Technol* 30(no. 11):1108–1117
- Castro TJ, Rodrigues PAM, Oliveira AC, Nakagomi F, Mantilla J, Coaquira JAH, Junior AF, Pessoni HVS, Morais PC, da Silva SW (2017) Optical and magnetic properties of Co-doped ZnO nanoparticles and the onset of ferromagnetic order. *J Appl Phys* 121(no. 1):013904
- Özgür Ü, Alivov YaI, Liu Chunli (2005) A comprehensive review of ZnO materials and devices *J Appl Phys* 98(no. 4):11. <https://doi.org/10.1063/1.1992666>
- Franco Jr A, Pessoni HVS, Ribeiro PRT, Machado FLA (2017) Magnetic properties of Co-doped ZnO nanoparticles. *J Magnetism Magn Mater* 426:347–350
- Chambers SA, Gallagher B (2008) Focus on dilute magnetic semiconductors. *New J Phys* 10(no. 5):055004
- Dietl Tomasz (2010) A ten-year perspective on dilute magnetic semiconductors and oxides. *Nat Mater* 9(no. 12):965
- Das S, Bandyopadhyay A, Saha P, Das S, Sutradhar S (2018) Enhancement of room-temperature ferromagnetism and dielectric response in nanocrystalline ZnO co-doped with Co and Cu. *J Alloys Compounds* 749:1–9
- Banerjee S, Mandal M, Gayathri N, Sardar M (2007) Enhancement of ferromagnetism upon thermal annealing in pure ZnO. *Appl Phys Lett* 91(no. 18):182501
- Gandhi V, Ganesan R, Syedahamed HHA, Thaiyan M (2014) Effect of cobalt doping on structural, optical, and magnetic properties of ZnO nanoparticles synthesized by coprecipitation method. *J Phys Chem C* 118(no. 18):9715–9725
- Vanaja A, Rao KS (2016) Effect of Co doping on structural and optical properties of zinc oxide nanoparticles synthesized by sol-gel method. *Adv Nanoparticles* 5(no. 01):83
- Gao Q, Dai Y, Li C, Yang L, Li X, Cui C (2016) Correlation between oxygen vacancies and dopant concentration in Mn-doped ZnO nanoparticles synthesized by co-precipitation technique. *J Alloys Compounds* 684:669–676
- Aljawf RN, Rahman F, Kumar S (2016) Defects/vacancies engineering and ferromagnetic behavior in pure ZnO and ZnO doped with Co nanoparticles. *Mater Res Bull* 83:108–115
- Koutu V, Shastri L, Malik MM (2017) Effect of temperature gradient on zinc oxide nano particles synthesized at low reaction temperatures. *Mater Res Express* 4(no. 3):035011
- Koutu V, Shastri L, Malik MM (2016) Effect of NaOH concentration on optical properties of zinc oxide nanoparticles. *Mater Sci Poland* 34(no. 4):819–827
- Ba-Abbad MM, Mohd ST, Benamor A, Abdul WM (2016) Synthesis and characterisation of Co<sup>2+</sup>-incorporated ZnO nanoparticles prepared through a sol-gel method. *Adv Powder Technol* 27(no. 6):2439–2447
- Chithra MJ, Pushpanathan K, Loganathan M (2014) Structural and optical properties of Co-doped ZnO nanoparticles synthesized by precipitation method. *Mater Manufacturing Process* 29(no. 7):771–779
- Godavarti U, Mote VD, Dasari M (2017) Role of cobalt doping on the electrical conductivity of ZnO nanoparticles. *J Asian Ceram Soc* 5(no. 4):391–396
- Ali RN, Naz H, Li J, Zhu X, Liu P, Xiang B (2018) Band gap engineering of transition metal (Ni/Co) codoped in zinc oxide (ZnO) nanoparticles. *J Alloys Compounds* 744:90–95
- Šutka As, Käämbre T, Pärna R, Juhnevicā I, Maiorov M, Joost U, Kisand V (2016) Co doped ZnO nanowires as visible light photocatalysts. *Solid State Sci* 56:54–62
- Bhatia S, Verma N (2017) Photocatalytic activity of ZnO nanoparticles with optimization of defects. *Mater Res Bull* 95:468–476
- Guruvammal D, Selvaraj S, Meenakshi Sundar S (2018) Structural, optical and magnetic properties of Co doped ZnO DMS nanoparticles by microwave irradiation method. *J Magnetism Magn Mater* 452:335–342
- Das S, Das S, Das D, Sutradhar S (2017) Tailoring of room temperature ferromagnetism and electrical properties in ZnO by Co (3d) and Gd (4f) element co-doping. *J Alloys Compounds* 691:739–749
- Aljawf RN, Rahman F, Kumar S (2016) Defects/vacancies engineering and ferromagnetic behavior in pure ZnO and ZnO doped with Co nanoparticles. *Mater Res Bull* 83:108–115
- Shatnawi M, Alsmadi AM, Bsoul I, Salameh B, Alna'washi GA, Al-Dweri F, El Akkad F (2016) Magnetic and optical properties of Co-doped ZnO nanocrystalline particles. *J Alloys Compounds* 655:244–252
- Ta QTH, Namgung G, Noh J-S (2018) Morphological evolution of solution-grown cobalt-doped ZnO nanostructures and their properties. *Chem Phys Lett* 700:1–6
- Sharma D, Jha R (2017) Analysis of structural, optical and magnetic properties of Fe/Co co-doped ZnO nanocrystals. *Ceram Int* 43(no. 11):8488–8496
- Saleh R, Prakoso SP, Fishli A (2012) The influence of Fe doping on the structural, magnetic and optical properties of nanocrystalline ZnO particles. *J Magnetism Magn Mater* 324(no. 5):665–670
- Doğan N, Bingölbali A, Arda L (2015) Preparation, structure and magnetic characterization of Ni doped ZnO nano-particles. *J Magnetism Magn Mater* 373:226–230
- Srinet G, Varshney P, Kumar R, Sajal V, Kulriya PK, Knobel M, Sharma SK (2013) Structural, optical and magnetic properties of Zn<sub>1-x</sub>CoxO prepared by the sol-gel route. *Ceram Int* 39(no. 6):6077–6085
- De Godoy MPF, Mesquita A, Avansi W, Neves PP, Chitta VrA, Ferraz WB, Boselli MA, Sabioni ACS, De Carvalho HB (2013) Evidence of defect-mediated magnetic coupling on hydrogenated Co-doped ZnO. *J Alloys Compounds* 555:315–319
- Koutu V, Subohi O, Shastri L, Malik MM (2018) Study the effect of dip in reaction temperature on thermal and electrical properties of ZnO nanoparticles. *Adv Powder Technol* 29(no. 9):2061–2069
- Debnath B, Halder G, Bhattacharyya S (2014) One-step synthesis, structural and optical characterization of self-assembled ZnO nanoparticle clusters with quench-induced defects. *Sci Adv Mater* 6(no. 6):1160–1169
- Cao W, Du W (2007) Strong exciton emission from ZnO microcrystal formed by continuous 532 nm laser irradiation. *J Luminescence* 124(no. 2):260–264
- Kumar H, Rani R (2013) Structural and optical characterization of ZnO nanoparticles synthesized by microemulsion route. *Int Lett Chem Phys Astron* 14:26–36
- Kumar S, Sahare PD (2012) Observation of band gap and surface defects of ZnO nanoparticles synthesized via hydrothermal route at different reaction temperature. *Optics Commun* 285(no. 24):5210–5216
- Kumbhakar P, Singh D, Tiwary CS, Mitra AK (2008) Chemical synthesis and visible photoluminescence emission from mono-dispersed ZnO nanoparticles. *Chalcogenide Lett* 5(no. 12):387–394